



The Discovery of a Planetary Companion Interior to Hot Jupiter WASP-132 b

Benjamin J. Hord^{1,2,3} , Knicole D. Colón^{2,3} , Travis A. Berger^{2,3,19} , Veselin Kostov^{2,3} , Michele L. Silverstein^{2,3,19} , Keivan G. Stassun⁴ , Jack J. Lissauer⁵ , Karen A. Collins⁶ , Richard P. Schwarz⁷ , Ramotholo Sefako⁸ , Carl Ziegler⁹ , César Briceño¹⁰ , Nicholas Law¹¹ , Andrew W. Mann¹¹ , George R. Ricker¹² , David W. Latham⁶ , S. Seager^{12,13,14} , Joshua N. Winn¹⁵ , Jon M. Jenkins⁵ , Luke G. Bouma¹⁶ , Ben Falk¹⁷ , Guillermo Torres⁶ , Joseph D. Twicken^{5,18} , and

Andrew Vanderburg¹²

¹ Department of Astronomy, University of Maryland, College Park, MD 20742, USA; benhord@astro.umd.edu

² NASA Goddard Space Flight Center, 8800 Greenbelt Road, Greenbelt, MD 20771, USA

³ GSFC Sellers Exoplanet Environments Collaboration, USA

⁴ Department of Physics and Astronomy, Vanderbilt University, Nashville, TN 37235, USA

⁵ NASA Ames Research Center, Moffett Field, CA 94035, USA

⁶ Center for Astrophysics | Harvard & Smithsonian, 60 Garden Street, Cambridge, MA 02138, USA

⁷ Patashnick Voorheesville Observatory, Voorheesville, NY 12186, USA

⁸ South African Astronomical Observatory, P.O. Box 9, Observatory, Cape Town 7935, South Africa

⁹ Department of Physics, Engineering and Astronomy, Stephen F. Austin State University, 1936 North Street, Nacogdoches, TX 75962, USA

¹⁰ Cerro Tololo Inter-American Observatory/NSF's NOIRLab, Casilla 603, La Serena, Chile

¹¹ Department of Physics and Astronomy, The University of North Carolina at Chapel Hill, Chapel Hill, NC 27599-3255, USA

¹² Department of Physics and Kavli Institute for Astrophysics and Space Research, Massachusetts Institute of Technology, Cambridge, MA 02139, USA

¹³ Department of Earth, Atmospheric and Planetary Sciences, Massachusetts Institute of Technology, Cambridge, MA 02139, USA

¹⁴ Department of Aeronautics and Astronautics, MIT, 77 Massachusetts Avenue, Cambridge, MA 02139, USA

¹⁵ Department of Astrophysical Sciences, Princeton University, 4 Ivy Lane, Princeton, NJ 08544, USA

¹⁶ Cahill Center for Astrophysics, California Institute of Technology, Pasadena, CA 91125, USA

¹⁷ Space Telescope Science Institute, 3700 San Martin Drive, Baltimore, MD 21218, USA

¹⁸ SETI Institute, Mountain View, CA 94043, USA

Received 2022 March 25; revised 2022 May 3; accepted 2022 May 11; published 2022 June 16

Abstract

Hot Jupiters are generally observed to lack close planetary companions, a trend that has been interpreted as evidence for high-eccentricity migration. We present the discovery and validation of WASP-132 c (TOI-822.02), a $1.85 \pm 0.10 R_{\oplus}$ planet on a 1.01 day orbit interior to the hot Jupiter WASP-132 b. Transiting Exoplanet Survey Satellite and ground-based follow-up observations, in conjunction with vetting and validation analysis, enable us to rule out common astrophysical false positives and validate the observed transit signal produced by WASP-132 c as a planet. Running the validation tools *vespa* and *TRICERATOPS* on this signal yields false-positive probabilities of 9.02×10^{-5} and 0.0107, respectively. Analysis of archival CORALIE radial velocity data leads to a 3σ upper limit of 28.23 ms^{-1} on the amplitude of any 1.01 day signal, corresponding to a 3σ upper mass limit of $37.35 M_{\oplus}$. Dynamical simulations reveal that the system is stable within the 3σ uncertainties on the planetary and orbital parameters for timescales of ~ 100 Myr. The existence of a planetary companion near the hot Jupiter WASP-132 b makes the giant planet's formation and evolution via high-eccentricity migration highly unlikely. Being one of just a handful of nearby planetary companions to hot Jupiters, WASP-132 c carries with it significant implications for the formation of the system and hot Jupiters as a population.

Unified Astronomy Thesaurus concepts: [Exoplanet astronomy \(486\)](#); [Exoplanet systems \(484\)](#); [Exoplanets \(498\)](#); [Hot Jupiters \(753\)](#); [Extrasolar gaseous planets \(2172\)](#); [Transit photometry \(1709\)](#)

1. Introduction

Ever since the Nobel Prize-winning discovery of the first exoplanet around a Sun-like star (Mayor & Queloz 1995), hot Jupiters have represented one of the greatest enigmas of exoplanet science. With radii $R_p > 8 R_{\oplus}$ and orbital periods $P < 10$ days (Winn et al. 2010; Wang et al. 2015; Garhart et al. 2020), hot Jupiters represent a class of planets with no analog in our solar system. Traditional theories on planet formation are insufficient to explain the existence of giant gaseous planets so close to a host star (Lin et al. 1996). Therefore, new formation

scenarios have been put forth (e.g., disk migration, planet-planet scattering, secular migration) to explain the existence of hot Jupiters, most of which involve an inward migration after initially forming beyond the ice line (e.g., Lin et al. 1996; Rasio & Ford 1996). However, none of these mechanisms alone can satisfy all observable constraints, leaving the primary pathways of hot Jupiter formation still largely uncertain (Dawson et al. 2014; Dawson & Johnson 2018).

One clue that may help distinguish between different formation pathways is that hot Jupiters are predominantly “lonely,” meaning they are the only planet in their system within a factor of 2 or 3 in orbital distance (e.g., Steffen et al. 2012; Endl et al. 2014; Knutson et al. 2014; Hord et al. 2021), although they may have more distant companions, particularly giant companions (Schlaufman & Winn 2016). This lack of nearby companions is expected from a high-eccentricity migration formation pathway, a scenario in which the hot

¹⁹ NASA Postdoctoral Program Fellow.

Jupiter migrates inward from beyond the ice line via some form of gravitational perturbations that put it on an eccentric orbit that eventually circularizes much closer to the host star (Rasio & Ford 1996). This high-eccentricity migration results in the scattering and possible ejection of other planets in the system as the hot Jupiter’s eccentric orbit sweeps through the inner parts of the stellar system (Mustill et al. 2015).

Of the ~ 500 hot Jupiters currently confirmed, only three have proven to be exceptions to this lonely trend so far. The systems WASP-47 (Becker et al. 2015), Kepler-730 (Cañas et al. 2019), and TOI-1130 (Huang et al. 2020) all host a hot Jupiter with at least one nearby companion planet, making the high-eccentricity migration scenario for these planetary systems unlikely.²⁰ It is more likely that these planetary systems formed via disk migration, where the protoplanets migrate inward all together within the disk, potentially preserving planets near the hot Jupiter (Lin et al. 1996; Lee & Peale 2002; Raymond et al. 2006). These systems serve as rare opportunities to dynamically constrain the formation of hot Jupiters and also potentially serve as a bridge to the slightly cooler population of warm Jupiters ($10 \text{ days} < P < 100 \text{ days}$), which are often joined by smaller companion planets (Huang et al. 2016). Hot Jupiters with nearby planets may be key in understanding the connection of formation pathways to the observed hot Jupiter population.

The Transiting Exoplanet Survey Satellite (TESS; Ricker 2015) is well suited to the discovery of hot Jupiters and potential nearby companions, as its almost-all-sky coverage is expected to observe nearly every known hot Jupiter system and discover hundreds or thousands more (Sullivan et al. 2015; Barclay et al. 2018). This is particularly important, since the hot Jupiter sample is currently heterogeneous and incomplete (Yee et al. 2021). In addition, TESS has the photometric precision to identify smaller planets down to $\sim 0.7 R_{\oplus}$ (e.g., Kostov et al. 2019b; Gilbert et al. 2020; Silverstein et al. 2022).

Here we present the TESS discovery of TOI-822.02, henceforth referred to as WASP-132 c, a small planet associated with the hot Jupiter WASP-132 b first discovered by Hellier et al. (2017). The new planet WASP-132 c is on a 1.01 day orbit interior to the 7.13 day orbit of the hot Jupiter WASP-132 b. This makes the WASP-132 system the fourth such system containing a hot Jupiter with a nearby small planetary companion, widening the sample of this rare subclass of hot Jupiters and further opening the possibility for comparative planetology both within the hot Jupiter system and between hot and warm Jupiter systems.

Section 2 details the discovery of the WASP-132 c signal in the TESS photometric data, as well as the initial vetting efforts. Section 3 presents our refinement of the stellar parameters of the host star using a series of independent models. Section 4 describes our methodology for modeling the full photometric light curve to obtain precise planetary and orbital parameters for WASP-132 c, as well as the confirmed hot Jupiter WASP-132 b. Section 5 presents the validation of WASP-132 c as a planet based on ground-based follow-up observations and

statistical validation software. Section 6 details the dynamical simulations modeling a two-planet WASP-132 system to probe the long-term stability of the system. Section 7 discusses the implications of the discovery of such a system in terms of hot Jupiter formation and the larger hot Jupiter sample.

2. Signal Search and Vetting

WASP-132 (TOI-822, TIC 127530399) was observed by TESS in Sector 11 from UT 2019 April 23 to May 20 (23.96 days) in CCD 2 of Camera 1 and in Sector 38 from UT 2021 April 29 to May 26 (26.34 days) in CCD 1 of Camera 1. Data for WASP-132 were collected at 2 minute cadence in Sectors 11 and 38 and 20 s cadence in Sector 38. The star was prioritized for high-cadence measurements as part of the Cycle 1 Guest Investigator Programs G011112, G011183, and G011132 and Cycle 3 Guest Investigator Programs G03278, G03181, and G03106.²¹

The TESS Science Processing Operation Center (SPOC) pipeline (Jenkins et al. 2016) processed the short-cadence pixel data and generated the target pixel files and light curves cleaned of instrumental systematics. The Transiting Planet Search module (TPS; Jenkins 2002; Jenkins et al. 2010, 2020) of the SPOC pipeline searched the generated 2 minute light curves for periodic, transit-like signals for each TESS sector independently and jointly as a single light curve. The TPS recovered the previously confirmed hot Jupiter WASP-132 b, as well as a new signal at 1.01153 days with a signal-to-noise ratio (S/N) of 10.6 in the combined data from the two sectors. This signal’s depth corresponds to a planet with a radius of $2.33 R_{\oplus}$ when using the stellar radius value for this target contained in the TESS Input Catalog (TICv8.2; Stassun et al. 2018, 2019) to calculate the potential planet radius. The transits of the hot Jupiter and WASP-132 c in the TESS data can be seen in Figure 1.

To provide an independent recovery of this periodic signal, we searched the available WASP-132 TESS light curves with the transit least-squares (TLS) search algorithm (Hippke & Heller 2019). TLS utilizes analytical transit shapes, making it more sensitive to planet transits than the conventional box least-squares (Kovács et al. 2002) search method and more finely tuned to detect small, short-period planets such as WASP-132 c.

Our transit search with TLS made use of the systematics-corrected Presearch Data Conditioning Simple Aperture Photometry (PDC_SAP) TESS light curves generated by the TESS SPOC pipeline (Smith et al. 2012; Stumpe et al. 2012, 2014) at the 2 minute and 20 s cadence for TESS Sectors 11 and 38, respectively.²² We used the `lightkurve` Python package (Lightkurve Collaboration et al. 2018) to download the data from the Mikulski Archive for Space Telescopes. The light curve exhibited small-amplitude stellar variability and was detrended using `lightkurve`’s built-in `flatten` method. A window length of >0.5 day was chosen, as it was both large enough to preserve transit signals (of duration on the order of $\lesssim 3$ hr) and small enough to remove the slight stellar variability present in the light curve.

²⁰ We note that WASP-148 b is a hot Jupiter with an outer massive companion at just within three times the orbital distance of the hot Jupiter. We choose not to include this system in our discussion of hot Jupiters with nearby companions because of its very different architecture from the other systems (which have smaller, closer companions) and because the mass and orbital distance of the companion planet put it on the borderline of the approximate definition of hot Jupiters with close planetary companions.

²¹ Details of the approved TESS Guest Investigator Programs are available from <https://heasarc.gsfc.nasa.gov/docs/tess/approved-programs.html>.

²² We elected to use the shortest cadence available for each sector to capture the shape of the transit as accurately as possible.

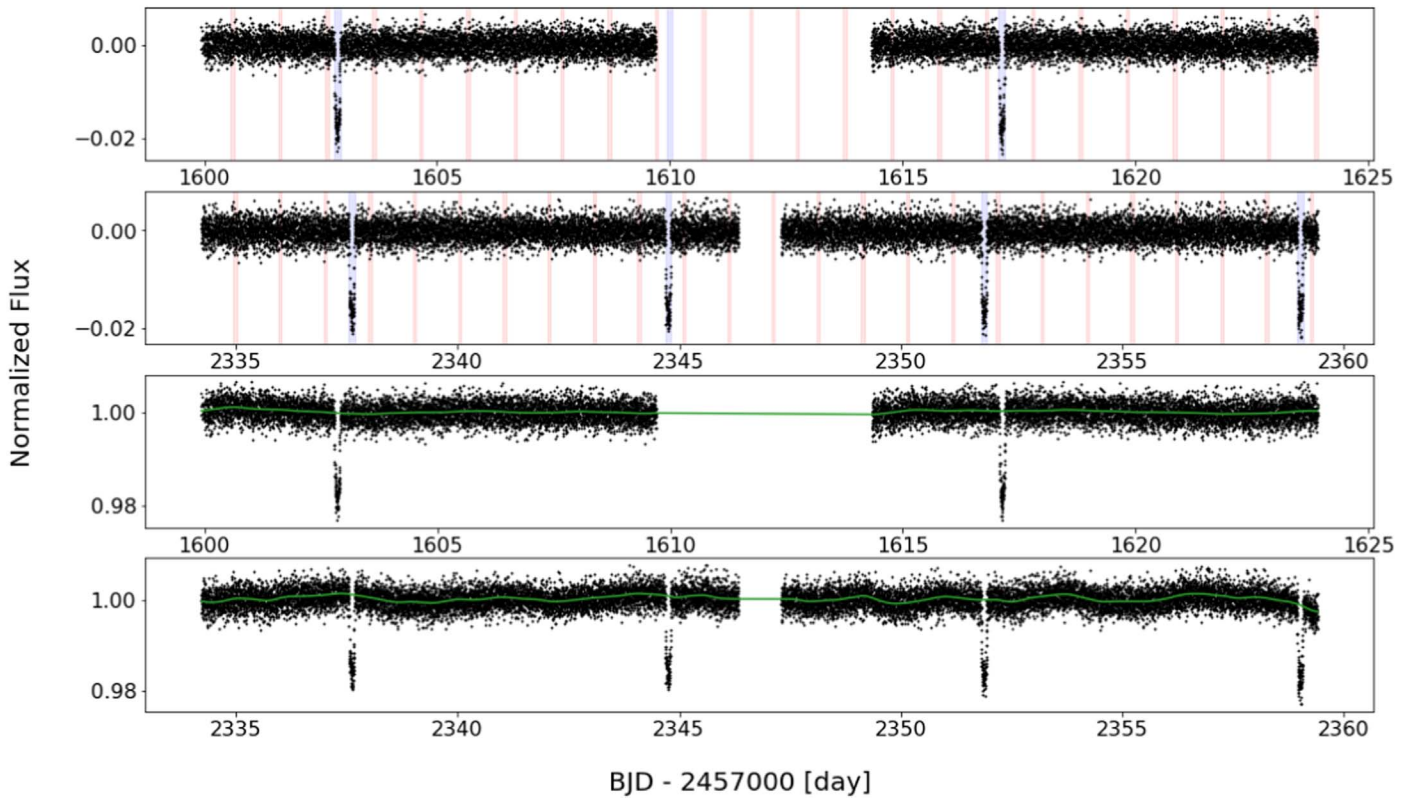


Figure 1. TESS PDC_SAP light curve of the WASP-132 system with the in-transit times of hot Jupiter WASP-132 b (blue) and WASP-132 (red) highlighted. Both Sector 11 (first panel) and Sector 38 (second panel) are shown. The data are detrended with a GP according to the method outlined in Section 4. These GP noise models are shown in green for Sector 11 (third panel) and Sector 38 (fourth panel) overlaid on the PDC_SAP light curves to show how they capture the variability in the light curve.

Using TLS on the clean light curve, we recovered the known signal of hot Jupiter WASP-132 b, as well as a signal with a period of 1.0119 ± 0.0032 days with a false-alarm probability (FAP) $< 10^{-4}$, which is well below the threshold of what Hippke & Heller (2019) stated is a significant detection above white noise. The period, depth, and mid-transit time of this recovered signal are consistent with the values reported by the SPOC pipeline and listed on the Exoplanet Follow-up Observing Program-TESS (ExoFOP-TESS; ExoFOP 2019) website.²³ This recovery with TLS served as an independent check to ensure that the signal was not a pipeline-specific detection.

We performed multiple initial checks of the signal and TESS light curves for astrophysical false-positive scenarios that can mimic exoplanet transits. The data validation (DV) module (Twicken et al. 2018; Li et al. 2019) of the SPOC pipeline performs a suite of diagnostic vetting tests to investigate the likelihood of many of these false-positive scenarios. These tests include a depth test of the odd and even transits, a statistical bootstrap test that accounts for the nonwhite nature of the light curve to estimate the probability of a false alarm from random noise fluctuations, a ghost diagnostic test to compare the detection statistic of the optimal aperture against that of a halo with a 1 pixel buffer around the optimal aperture, and a difference image centroid test. WASP-132 c passed all of these diagnostic vetting tests. Additionally, all TICv8.2 objects other than the target star were statistically excluded as sources of the 1.01 day transit signal, since the difference centroid offset tests

located the source of the transit signal to within $1'' \pm 3''$ of the target position. The threshold crossing event was promoted to TESS object of interest (TOI; Guerrero et al. 2021) status and designated TOI-822.02 by the TESS Science Office based on the clean model fit and diagnostic test results in the SPOC DV report.

In addition to the vetting checks performed by the SPOC pipeline, we used Discovery and Vetting of Exoplanets (DAVE; Kostov et al. 2019a) to further check for astrophysical false-positive scenarios. DAVE is an automated vetting pipeline built upon many of the tools developed for vetting planets in Kepler data (e.g., RoboVetter; Coughlin et al. 2014). It has been used extensively in vetting planets in K2 (Hedges et al. 2019; de Leon et al. 2021) and TESS (Crossfield et al. 2019; Kostov et al. 2019b; Gilbert et al. 2020) data as well. DAVE performs two sets of vetting tests. The first are light curve-based vetting tests searching for odd/even transit differences, secondary eclipses, and light-curve modulations that could introduce transit-like signals. The second set of tests are image-based and check the photocenter motion on the TESS image during transit.

Unfortunately, due to the weak signal resulting from the shallow transit depth and relatively dim ($T_{\text{mag}} = 11.11$) stellar host, many of the results from DAVE were inconclusive but still showed no significant indication of an astrophysical false-positive scenario. As such, we determined that further, more detailed modeling of the transits was warranted.

²³ <https://exofop.ipac.caltech.edu/tess/>

Table 1
Stellar Parameters Obtained Using Each of the Methods Outlined in Section 3

Parameter	TICv8.2	Hellier et al. (2017)	Isochrone Analysis	KGS SED Analysis	MLS SED Analysis
T_{eff} (K)	4742 ± 129	4750 ± 100	4714^{+87}_{-88}	4750 ± 75	4753 ± 80
[Fe/H]	...	0.22 ± 0.13	0.18 ± 0.12	0.0 ± 0.5	...
M_* (M_{\odot})	0.760 ± 0.089	0.80 ± 0.04	0.782 ± 0.034	0.80 ± 0.05	...
R_* (R_{\odot})	0.790 ± 0.057	0.74 ± 0.02	$0.753^{+0.028}_{-0.026}$	0.752 ± 0.024	0.767 ± 0.026
L_* (L_{\odot})	0.284 ± 0.012	...	$0.253^{+0.032}_{-0.028}$...	0.271 ± 0.007
$\log(g)$	4.524 ± 0.094	4.6 ± 0.1	$4.576^{+0.028}_{-0.036}$
ρ_* (g cm^{-3})	2.17 ± 0.59	$2.82^{+0.10}_{-0.20}$	$1.81^{+0.18}_{-0.19}$
Age (Gyr)	...	$\gtrsim 0.5$	$7.055^{+7.114}_{-5.000}$	3.2 ± 0.5	...
Distance (pc)	122.91 ± 0.57	120 ± 20	126 ± 5
F_{bol} ($\text{erg s}^{-1} \text{cm}^{-2} \times 10^{-10}$)	5.442 ± 0.063	5.69 ± 0.14

Note. Values from Hellier et al. (2017), who discovered WASP-132 b, and from the TICv8.2 (Stassun et al. 2018, 2019) are included for comparison. The final adopted parameters for this analysis are contained in Table 2. All uncertainties reported are the 1σ value.

3. Refinement of Host Star Parameters

To perform a comprehensive analysis of the transit and system light curve, it was necessary to refine the stellar parameters of the host star, WASP-132. The TICv8.2 reports key stellar parameters determined via independent analysis, but there are also stellar parameters reported by the WASP Collaboration in the initial discovery and confirmation of the hot Jupiter WASP-132 b (Hellier et al. 2017). We performed our own independent analysis given the available data in order to determine the best values for the stellar parameters to use when modeling the TESS data. The results of each independent analysis method are contained in Table 1 for comparison. We find that most stellar parameter values from each analysis method are consistent with each of the others, as well as with those reported by both Hellier et al. (2017) and the TICv8.2 (Stassun et al. 2018, 2019). The exception is a slight difference between the bolometric flux F_{bol} reported by the two spectral energy distribution (SED) analyses. The adopted stellar parameter values used in the remaining validation and analysis of WASP-132 c are based on the isochrone analysis described below and contained in Table 2.

We also note that we see a low-amplitude 8 day periodic variation upon visual inspection of the Sector 38 light curve that does not match up with the 33 day stellar rotation period stated in Hellier et al. (2017). If the 8 day variability were to represent the rotation period of the star, this would imply a $v \sin i$ of $\sim 5 \text{ km s}^{-1}$, using the equation $v \sin i = (2\pi R)/P$ and assuming the star is viewed edge-on. This is well outside of the confidence interval of the measured value $v \sin i = 0.9 \pm 0.8 \text{ km s}^{-1}$, suggesting that this 8 day variability is not the stellar rotation period, although it may represent one of the harmonics of the true period if it is intrinsic to the star. However, extracted light curves using different apertures do not contain this ~ 8 day variation, suggesting that this shorter-scale variability may not be inherent to the WASP-132 system. Regardless of the origin of this additional variability, our conclusions remain the same regarding the planetary nature of the 1.01 day transit signal.

Overall, WASP-132 does not show significant signs of activity. There is the possible 8 day variability and reported 33 day rotation period, activity that occurs on much longer timescales than the orbital period of WASP-132 c. We also found no evidence of flares or starspot crossings in either the space- or ground-based data. In the modeling of the system's light curves (see Section 4), a Gaussian process (GP) was used

to capture any variability in conjunction with transit models for each planet. Thus, photometric variability was modeled out while not diluting the transit signals (see Figure 1) in order to precisely measure the planet and orbital parameters.

3.1. Isochrone Analysis

We performed an isochrone-based analysis for WASP-132 using `isoclassify` (Huber et al. 2017; Berger et al. 2020), which produces fundamental stellar parameters from a combination of input observables. We used spectroscopic T_{eff} and metallicity from the discovery paper (Hellier et al. 2017), Gaia Data Release 2 (DR2; Prusti et al. 2016; Bailer-Jones et al. 2018; Gaia Collaboration et al. 2018) parallax and coordinates, and the Two Micron All-Sky Survey (2MASS; Skrutskie et al. 2006) K_s magnitude as inputs. We also used the `allsky` extinction map detailed in Bovy et al. (2016) to estimate the photometric extinction based on the coordinates and distance inferred from the parallax. The best-fit values and their uncertainties are compiled in Table 1, and we estimate the extinction to be $A_V = 0.097 \pm 0.024 \text{ mag}$, which is consistent with the $A_V = 0.093 \pm 0.031 \text{ mag}$ reported in the TICv8.2.

3.2. KGS SED Analysis

As an independent determination of the basic stellar parameters, K. G. Stassun (KGS) performed an analysis of the broadband SED of the star, together with the Gaia Early Data Release 3 (EDR3; Prusti et al. 2016; Brown et al. 2021) parallax (with no systematic offset applied; see, e.g., Stassun & Torres 2021), in order to determine an empirical measurement of the stellar radius, following the procedures described in Stassun & Torres (2016) and Stassun et al. (2017, 2018). We pulled the JHK_S magnitudes from 2MASS, the W1–W3 magnitudes from the Wide-field Infrared Survey Explorer (WISE; Wright et al. 2010; Cutri et al. 2013), and the $G_{\text{BP}}G_{\text{RP}}$ magnitudes from Gaia. Together, the available photometry spans the full stellar SED over the wavelength range 0.4–10 μm (see Figure 2).

We performed a fit using NextGen stellar atmosphere models, with the free parameters being the effective temperature (T_{eff}) and metallicity ([Fe/H]), as well as the extinction A_V , which we fixed at zero due to the proximity of the system to Earth. The resulting fit (Figure 2) has a best-fit $T_{\text{eff}} = 4750 \pm 75 \text{ K}$, $[\text{Fe}/\text{H}] = 0.0 \pm 0.5$, with a reduced χ^2 of 0.8. Integrating the (unreddened) model SED gives the

Table 2
Adopted Stellar Parameters for WASP-132

Parameter	Value	Source
Identifying Information		
Name	WASP-132	
TIC ID	127530399	TICv8.2
TOI ID	TOI-822	Guerrero et al. (2021)
Alt. Name	UCAC4 220-083803	
Astrometric Properties		
α R.A. (hh:mm:ss)	14:30:26.21 (J2015.5)	Gaia EDR3
δ decl. (dd:mm:ss)	-46:09:34.29 (J2015.5)	Gaia EDR3
μ_α (mas yr ⁻¹)	12.255 ± 0.020	Gaia EDR3
μ_δ (mas yr ⁻¹)	-73.169 ± 0.022	Gaia EDR3
Distance (pc)	123.57 ± 0.29	Gaia EDR3
Stellar Properties		
Spectral type	K4	Hellier et al. (2017)
T_{eff} (K)	4714 ⁺⁸⁷ ₋₈₈	This work
[Fe/H]	0.18 ± 0.12	This work
M_* (M_\odot)	0.782 ± 0.034	This work
R_* (R_\odot)	0.753 ^{+0.028} _{-0.026}	This work
L_* (L_\odot)	0.253 ^{+0.032} _{-0.028}	This work
log(g)	4.576 ^{+0.028} _{-0.036}	This work
ρ_* (g cm ⁻³)	1.81 ^{+0.18} _{-0.19}	This work
Rotation period (days)	~33	Hellier et al. (2017)
$v \sin i$ (km s ⁻¹)	0.9 ± 0.8	Hellier et al. (2017)
Age (Gyr)	3.2 ± 0.5	This work
Photometric Properties		
B (mag)	13.142 ± 0.011	APASS DR9
V (mag)	11.938 ± 0.046	APASS DR9
G_G (mag)	11.7467 ± 0.0002	Gaia EDR3
G_{BP} (mag)	12.3000 ± 0.0007	Gaia EDR3
G_{RP} (mag)	11.0487 ± 0.0004	Gaia EDR3
T (mag)	11.111 ± 0.006	TICv8.2
J (mag)	10.257 ± 0.026	2MASS
H (mag)	9.745 ± 0.023	2MASS
K_s (mag)	9.674 ± 0.024	2MASS
W_1 (mag)	9.557 ± 0.022	AllWISE
W_2 (mag)	9.638 ± 0.020	AllWISE
W_3 (mag)	9.575 ± 0.040	AllWISE
W_4 (mag)	8.281 ^a	AllWISE

Note. Gaia EDR3: Prusti et al. (2016); Brown et al. (2021). TICv8.2: Stassun et al. (2019). APASS DR9: Henden et al. (2016). 2MASS: Skrutskie et al. (2006). AllWISE: Cutri et al. (2013).

^a Only a limit is reported for W_4 , since the S/N was too low for a confident detection.

bolometric flux at Earth, $F_{\text{bol}} = 5.442 \pm 0.063 \times 10^{-10}$ erg s⁻¹ cm⁻². Taking the F_{bol} and T_{eff} together with the Gaia parallax gives the stellar radius, $R_* = 0.752 \pm 0.024 R_\odot$. In addition, we can estimate the stellar mass from the empirical relations of Torres et al. (2010), giving $M_* = 0.80 \pm 0.05 M_\odot$. Finally, the reported stellar rotation period of ~33 days implies an age of $\tau_* = 3.2 \pm 0.5$ Gyr via the empirical gyrochronology relations of Mamajek & Hillenbrand (2008).

3.3. MLS SED Analysis

As an additional check on our stellar effective temperature, luminosity, and radius results, M. L. Silverstein (MLS) led a second SED analysis following methodology similar to that of

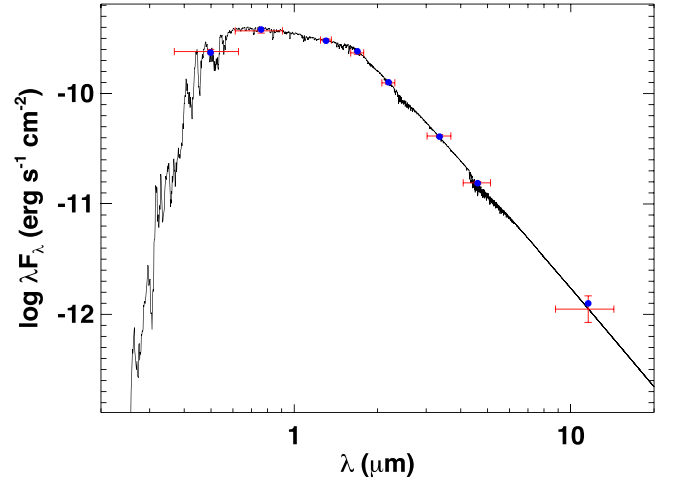


Figure 2. The SED of WASP-132. Red symbols represent the observed photometric measurements outlined in Section 3.2, where the horizontal bars represent the effective width of the passband. Blue symbols are the model fluxes from the best-fit NextGen atmosphere model (black).

Dieterich et al. (2014; Silverstein et al., in preparation). Spanning optical to mid-infrared wavelengths, we extract JHK_S magnitudes from 2MASS and $W1$ – $W3$ magnitudes from WISE as in the previous subsection. We differ in our adoption of the Gaia DR2 parallax and VRI photometry converted from Gaia DR2 $G_G G_{BP} G_{RP}$. We compare nine different color combinations to the BT-Settl 2011 photospheric models (Allard et al. 2012) to derive a best-fitting $T_{\text{eff}} = 4753 \pm 80$ K, assuming $[\text{Fe}/\text{H}] = 0$. Next, we iteratively scale the resulting best-match model using a polynomial function until the model and observed photometry match to within the error bars. We then integrate the final spectrum and apply a bolometric correction to determine $F_{\text{bol}} = 5.691 \pm 0.137 \times 10^{-10}$ erg s⁻¹ cm⁻², and we scale by the parallax to derive $L_* = 0.271 \pm 0.007 L_\odot$. A radius of $R_* = 0.767 \pm 0.026 R_\odot$ is then calculated using the Stefan–Boltzmann law. These results are listed in Table 1 and match those from the other independent methods described in this paper.

4. Modeling the Physical Properties of WASP-132 c

While TLS is useful at detecting signals, the period grid that it searches is not very fine by default. Combined with the refined stellar parameters discussed in Section 3, it is possible to model the light curve in a more detailed fashion than the initial transit search to find the maximum-likelihood values for the planet properties in the system. To perform this detailed modeling, we used the software *exoplanet* (Foreman-Mackey et al. 2019), a toolkit for probabilistic modeling of transit and radial velocity observations of exoplanets using PyMC3. This is a powerful and flexible program that can be used to build high-performance transit models and then sample them through Markov Chain Monte Carlo simulations to provide precise transit and orbital parameters.

We utilized the same PDC_SAP light curves used in the transit search with TLS with one difference. For the modeling with *exoplanet*, we did not apply any initial detrending that could possibly alter the transit signals but instead included a GP in the model. Our model had three elements: two planet components with Keplerian orbits and limb-darkened transits (one for each potential planet in the system) and a GP component that modeled residual stellar variability. The planet

models were computed using STARRY (Luger et al. 2019), and the GP was computed using `celerite` (Foreman-Mackey et al. 2017; Foreman-Mackey 2018). The GP component models the residual stellar variability in the light curve and describes a stochastically driven, damped harmonic oscillator with two hyperparameters, $\ln(S_0)$ and $\ln(\omega_0)$, which represent the undamped angular frequency of a simple harmonic oscillator and the power at $\omega=0$, respectively. We fixed the quality factor Q of the simple harmonic oscillator to $1/\sqrt{2}$ and put wide Gaussian priors on $\ln(S_0)$ and $\ln(\omega_0)$, setting their means to the natural log of the standard deviation of the flux and natural log of one-tenth of a cycle, respectively, with both of their standard deviations set to 10. This form of GP has the advantage of being able to model a wide range of low-frequency astrophysical and instrumental signals without requiring a physical model for the observed variability. We also included a white-noise term in the model that is parameterized by the natural log of the standard deviation of the flux with a prior identical to that of $\ln(S_0)$. The GP parameters of the two TESS sectors were modeled separately, since the sectors may have different noise parameters, especially since the data were taken at different cadences.

The planet model was parameterized with a two-term limb-darkening component and the stellar radius and mass. The individual planets were parameterized in terms of the natural log of orbital period, mid-transit time, transit depth, impact parameter, eccentricity, and periastron angle at the time of transit. For our priors on the stellar parameter components of the model, we used the mean and standard deviation values of our analysis discussed in Section 3 and displayed in Table 2. We followed Kipping (2013a) for the parameterization of the limb darkening. We used the SPOC values listed on ExoFOP-TESS for the means and standard deviations of Gaussian priors on the natural log of the orbital period, mid-transit time, and transit depth for the two planets. We imposed a uniform prior on the impact parameter bounded between zero and 1. For the eccentricity prior, we used a beta prior with $\alpha=0.867$ and $\beta=3.03$, as suggested by Kipping (2013b). The eccentricity was bounded between zero and 1 and sampled as $e\cos(\omega)$. The periastron angle at transit was sampled in vector space to avoid the sampler seeing discontinuities. We sampled the posterior distribution of the model parameters using the No U-turn Sampler (Hoffman et al. 2014), which is a form of Hamiltonian Monte Carlo, as implemented by `PYMC3` (Salvatier et al. 2016). We ran three simultaneous chains, each with 2000 tuning steps and 2500 draws in the final sample.

Initially, since individual TESS sectors often have different noise properties, we modeled both Sectors 11 and 38 independently from one another using the model described above. However, the resulting posterior distributions were equivalent within 1σ errors, so we decided to combine both sectors of TESS data into a single light curve and use the same model. Since the two light curves are separated by >1 yr, modeling both together as a single light curve increases the time baseline with which to model the orbit of the system, allowing for a better-constrained orbital period than any individual sector or two sectors back-to-back in time. We binned the Sector 38 TESS data from a 20 s cadence to a 2 minute cadence to match with the TESS Sector 11 data in order to create a uniform data set with an increased photometric precision in Sector 38. No correction for contamination from nearby sources of constant brightness was included, since

Table 3
Planet and Orbital Parameters for WASP-132 b and c Calculated by Modeling the TESS Photometric Data with `exoplanet`

Parameter	Value
Model Parameters	
Star	
Limb darkening u_1	0.43 ± 0.11
Limb darkening u_2	0.17 ± 0.24
Radius [R_\odot]	0.754 ± 0.024
Mass [M_\odot]	0.781 ± 0.033
$\ln(\rho_{\text{GP}})$	1.03 ± 0.15
$\ln(\sigma_{\text{GP}, S11})$	-7.96 ± 0.16
$\ln(\sigma_{\text{GP}, S38})$	-7.11 ± 0.16
WASP-132 c	
T_0 (BJD - 2,457,000)	$1,597.5762 \pm 0.0024$
$\ln(\text{period})$ [days]	$0.011 \pm 4.69\text{e-}6$
Impact parameter	$0.28^{+0.24}_{-0.19}$
$\ln(\text{transit depth})$	-7.437 ± 0.068
Eccentricity	$0.13^{+0.20}_{-0.09}$
ω [rad]	$-0.93^{+1.83}_{-1.65}$
WASP-132 b	
T_0 (BJD - 2,457,000)	$2,337.6080 \pm 0.0002$
$\ln(\text{period})$ [days]	$1.96 \pm 5.49\text{e-}7$
Impact parameter	0.16 ± 0.11
$\ln(\text{transit depth})$	-4.026 ± 0.01
Eccentricity	$0.07^{+0.15}_{-0.05}$
ω [rad]	$-0.08^{+2.55}_{-2.67}$
Derived Parameters	
WASP-132 c	
Period [days]	1.011534 ± 0.000005
R_p/R_*	0.023 ± 0.001
Radius [R_\oplus]	1.85 ± 0.10
Radius [R_J]	0.165 ± 0.009
a/R_*	5.17 ± 0.18
a [au]	0.0182 ± 0.0003
Inclination [deg]	$86.64^{+1.12}_{-3.52}$
Duration [hr]	$1.47^{+0.14}_{-0.22}$
WASP-132 b	
Period [days]	7.133514 ± 0.000004
R_p/R_*	0.122 ± 0.006
Radius [R_\oplus]	10.05 ± 0.34
Radius [R_J]	0.897 ± 0.030
a/R_*	19.03 ± 0.66
a [au]	0.067 ± 0.001
Inclination [deg]	$89.51^{+0.14}_{-0.49}$
Duration [hr]	$3.18^{+0.18}_{-0.21}$

Note. Errors are reported at the 1σ level. Noise parameters are also included.

follow-up observations by the Southern Astrophysical Research (SOAR) telescope and the Las Cumbres Observatory Global Telescope (LCOGT) cleared the nearby field of contaminating sources of this nature (see Section 5.1).

The median values and 1σ errors for the best-fit transit model are contained in Table 3, and the folded light curve with the best-fit and 1σ bounds of the transit model are shown in Figure 3.

5. Validation of WASP-132 c

While the TESS pipeline and DAVE perform vetting analyses against possible false-alarm and false-positive scenarios, they alone are not rigorous enough to validate the planetary nature

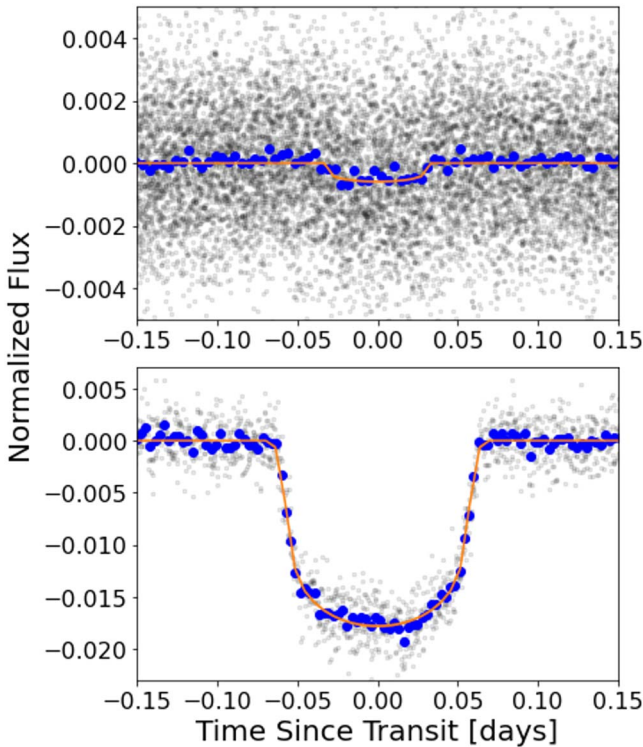


Figure 3. TESS data (light gray) for WASP-132 c (top) and WASP-132 b (bottom) phase-folded to the best-fit period and mid-transit time with the `exoplanet` model overlaid. The process of fitting the transit model is described in Section 4. The blue points are the phase-folded photometric data binned for clarity.

of WASP-132 c. We therefore investigated this signal using both observational constraints (Section 5.1) and the publicly available statistical software packages `vespa` and `TRICERA-TOPS` (Section 5.2).

5.1. Follow-up Observations

In order to better constrain the false-positive probability (FPP) of a planet candidate, follow-up observations can rule out sections of the parameter space of different astrophysical false-positive scenarios. Since WASP-132 is already known to host a confirmed hot Jupiter, both speckle imaging and radial velocity follow-up observations were readily available for our analysis and could be included in our final validation of WASP-132 c.

5.1.1. SOAR Speckle Imaging

High angular resolution imaging is needed to search for nearby sources that can contaminate the TESS photometry (resulting in an underestimated planetary radius) or be the source of astrophysical false positives, such as background eclipsing binaries. We searched for stellar companions to WASP-132 with speckle imaging using the HRCam instrument on the 4.1 m SOAR telescope (Tokovinin 2018) on 2020 February 10 UT, observing in the Cousins *I* band, a similar visible bandpass as TESS. This observation was sensitive to a 5.0 mag fainter star at an angular distance of $1''$ from the target. More details of the observation are available in Ziegler et al. (2020). The 5σ detection sensitivity and speckle autocorrelation functions from the observations are shown in Figure 4. No

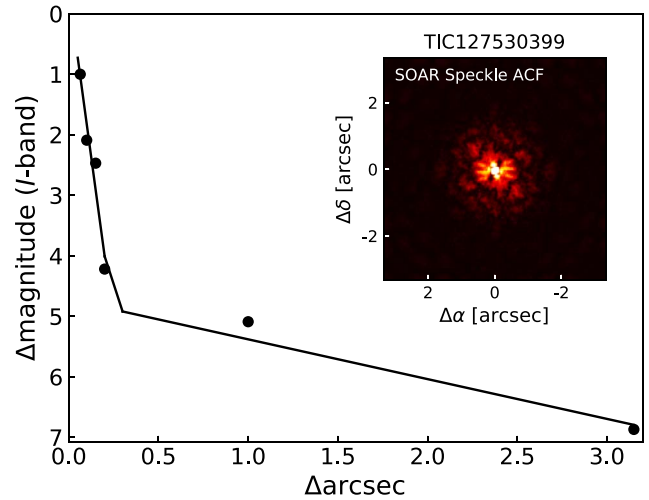


Figure 4. The 5σ detection sensitivity of the SOAR speckle imaging of WASP-132, with an inset two-dimensional autocorrelation function reconstructed image of the field. The data indicate that there are no close-in companions within $3''$ of WASP-132.

nearby stars were detected within $3''$ of WASP-132 in the SOAR observations.

5.1.2. CORALIE Radial Velocity Observations

In addition to SOAR speckle imaging, prior to the discovery of WASP-132 c, there already existed radial velocity measurements of the host star WASP-132 that were used to confirm the planetary nature and measure the mass of the hot Jupiter WASP-132 b. In total, there were 36 radial velocity measurements taken across a time span of almost 2 yr. All of these measurements were obtained with the CORALIE spectrograph, which is an echelle spectrograph mounted on the 1.2 m Euler telescope in La Silla, Chile. These data are published in Hellier et al. (2017), who provided further information regarding the method used to reduce the radial velocity data.

According to the `forecaster` Python package (Chen & Kipping 2016), the projected mass of WASP-132 c should be $4.45 M_{\oplus}$. The `forecaster` package assumed a gaseous envelope when estimating the mass of WASP-132 c; however, the radius of the planet may place it in the super-Earth regime of planets. This would imply that the density of the planet is higher than a gaseous planet, meaning that the mass follows the relation $M_p \sim R_p^{3.7}$. This would result in a mass of $9.74 M_{\oplus}$. We made no distinction between these two scenarios in our analysis of CORALIE data, since we imposed a very wide prior on the mass of WASP-132 c.

We first performed a joint fit of the time series TESS photometry with the CORALIE radial velocity measurements using `exoplanet`. This way, we were able to take advantage of the unique strengths of each data type in constraining the orbital and planetary parameters, as well as accounting for the noise and variability in the data. We used a model similar to that described in Section 4 but with the addition of planet mass, as well as a quadratic trend and a jitter term for the radial velocities. The priors on the trend and jitter model components were normal distributions, with the quadratic trend distribution centered on zero and the jitter term distribution centered on the standard deviation of the radial velocity data. We imposed a wide log-uniform prior on the mass from zero to 8. This is more

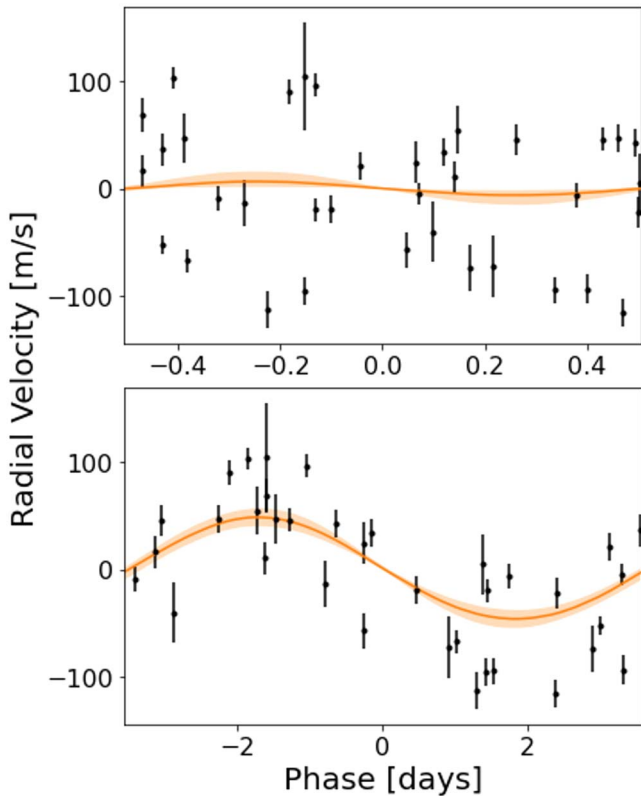


Figure 5. CORALIE radial velocity measurements phase-folded to the best-fit periods of WASP-132 c (top) and WASP-132 b (bottom). The solid orange line represents the median radial velocity model, and the shaded regions represent the 1σ uncertainties in the model.

than wide enough to encompass the projected masses of both potential compositions for WASP-132 c, as well as the 3σ upper limit on the reported mass of WASP-132 b. CORALIE also underwent an upgrade partway through the data set, and this is accounted for by an offset between the pre- and postupgrade portions of the data. We also fit for the trend in the data described in Hellier et al. (2017).

The posterior probability distribution for the mass of WASP-132 c was highest around zero with a wide spread of values, indicating a nondetection in the radial velocity. Therefore, we report a 3σ upper limit from this distribution of $37.35 M_{\oplus}$, corresponding to a radial velocity semiamplitude of 28.23 ms^{-1} . All other planetary and orbital parameters modeled with the joint TESS + CORALIE data (e.g., period, mid-transit time, radius, etc.) are consistent with the values obtained from modeling the TESS data alone, described in Section 4. The best-fit models are plotted with the phase-folded radial velocity data for WASP-132 b and c in Figure 5. We note that Hellier et al. (2017) reported that the CORALIE radial velocities show excess scatter, which may be due to magnetic activity. Therefore, the upper limit on the mass reported here may be inflated due to the high scatter.

As a check on the validity of the procedure, we also compared the measured planet mass for the confirmed hot Jupiter in the system WASP-132 b against its reported mass in Hellier et al. (2017). We measure the mass to be $121.89 \pm 21.85 M_{\oplus}$, which is in agreement with the $130.31 \pm 9.53 M_{\oplus}$ measured by Hellier et al. (2017). The uncertainty on our calculated mass of the hot Jupiter is higher than that reported by Hellier et al. (2017), likely because

Hellier et al. (2017) also joint fit the CORALIE data with photometric data from both Wide Angle Search for Planets (WASP) and TRANSiting Planets and Planetesimals Small Telescope (TRAPPIST) observations that our analysis does not include, as well as other ancillary radial velocity observation data products.

As an independent check of the values obtained from `exoplanet`, we used the online Data and Analysis Center for Exoplanets²⁴ platform to model the radial velocity data and investigate the significance of any signals around 1.01 days (the period of WASP-132 c). The Keplerian model initial conditions for the hot Jupiter were input based on the values on ExoFOP-TESS for WASP-132 b, and a decrease of 60 ms^{-1} over the course of the observations was added as noted in Hellier et al. (2017). When viewing the periodogram of the radial velocity data after adding in these components, there appear to be spikes in the signal around 1 day, none of which has an FAP $< 10\%$. This is not surprising, since many signals are aliased to 1 day, and this is a common phenomenon in analyzing radial velocity data. The addition of another Keplerian orbit at the expected orbital period of WASP-132 c with the predicted semiamplitude based on the mass predicted by `forecaster` results in a higher reduced χ^2 , indicating a worse fit.

According to Equation (14) in Lovis & Fischer (2011), the expected semiamplitude of the radial velocity signal of WASP-132 c with $4.45 M_{\oplus}$ as predicted by `forecaster` is 3.36 ms^{-1} . If an Earth-like composition is assumed, the mass of $9.74 M_{\oplus}$ would result in a semiamplitude of 7.44 ms^{-1} . CORALIE has been reported to have an individual measurement precision ranging between 3.5 and 6 ms^{-1} (Rickman et al. 2019), putting the projected mass of WASP-132 c slightly below and slightly above the lower limit of CORALIE’s detectable parameter space for gaseous and Earth-like compositions, respectively. Combined with the fact that the orbital period falls very close to the highly aliased value of 1 day, it is logical that there was no significant detection of WASP-132 c in the CORALIE radial velocity data. Further radial velocity observations are necessary with a more precise instrument, such as the High Accuracy Radial velocity Planet Searcher (HARPS) or the Carnegie Planet Finder Spectrograph (PFS), in order to obtain a mass measurement for the planet WASP-132 c.

5.1.3. LCOGT 1 m

We observed TOI-822 c from the LCOGT (Brown et al. 2013) 1.0 m network node at the South African Astronomical Observatory on UTC 2022 March 5, 2022 March 8, and 2022 March 9 in the Sloan i' band. We used the TESS Transit Finder, which is a customized version of the Tapir software package (Jensen 2013), to schedule our transit observations. The 1 m telescopes are equipped with 4096×4096 SINISTRO cameras having an image scale of $0''.389 \text{ pixel}^{-1}$, resulting in a $26' \times 26'$ field of view. The images were calibrated by the standard LCOGT BANZAI pipeline (McCully et al. 2018). Photometric data were extracted using `AstroImageJ` (Collins et al. 2017). The target star apertures exclude virtually all of the flux from the nearest Gaia EDR3 and TIC known neighbor (TIC 1051778874), which is

²⁴ <https://dace.unige.ch>

10''0 northwest of TOI-822. The light-curve data are available on the ExoFOP-TESS website²⁵ (ExoFOP 2019).

The UTC 2022 March 5 observation used focused observations that were intended to saturate the target star for purposes of checking fainter stars within 2/5 of TOI-822 c for a potential nearby eclipsing binary (NEB) that could be the cause of the periodic detection in the TESS data. We rule out NEB signals, relative to the depth required in each neighboring star given its TIC version 8 delta TESS magnitude, by a factor of more than three times the rms of the light-curve scatter for all neighboring stars out to 50'' from TOI-822. This is consistent with the SPOC pipeline's (lack of) centroid offset finding that the source of the TESS-detected signal is within $\sim 10''$ of the target star location using data from TESS Sectors 11 and 38. We also do not see any obvious NEB signals in stars out to 2/5, although some light curves suffer from blending from brighter nearby stars.

Although we expected the target star to be saturated in the UTC 2022 March 5 observation, it ultimately was strongly exposed but not saturated. While the detrended light curve is consistent with a 40 minute (2.7σ) late ~ 600 ppm deep event on target relative to the SPOC Sectors 11 and 38 ephemeris, the detection is considered inconclusive due to limited post-transit baseline coverage and apparent systematics at the level of ~ 500 ppm in the undetrended light curve.

The UTC 2022 March 8 and UTC 2022 March 9 observations were intentionally defocused to attempt to confirm the tentative 2.7σ late ~ 600 ppm deep event in the UTC 2022 March 5 data. However, these data also suffered from ~ 500 ppm systematics in the undetrended light curves. With our best detrending efforts, UTC 2022 March 8 would marginally suggest a roughly 100 minute late ~ 600 – 700 ppm deep ingress at the end of the light curve. On the other hand, the UTC 2022 March 9 detrended light curve would suggest a roughly 20 minute early ~ 700 ppm deep event.

Given the level of systematics in the undetrended data and the inconsistent timing of the three tentative transit detections in the detrended data, we do not further consider the on-target results in the following analyses. Although we favor the interpretation that the extracted events are systematics-driven, we cannot rule out the interpretation that some or all of the tentative detections are astrophysical and that the timing offsets are indicative of large transit timing variations (TTVs) in the system.

5.2. Validation Using Software Tools

While observational constraints can rule out portions of the parameter space where astrophysical false positives could exist, these observational limits are incomplete and do not rule out the entirety of the false-positive parameter space. We are able to statistically analyze the remaining likelihood of false-positive signals using publicly available software. Using the available follow-up observations as constraints, we ran *vespa* (Morton 2012, 2015) and TRICERATOPS (Giacalone & Dressing 2020; Giacalone et al. 2021) to further establish the planetary nature of this signal.

vespa compares the transit signal to a number of astrophysical false positives, including an unblended eclipsing binary, a blended background eclipsing binary, a hierarchical companion eclipsing binary, and eclipsing binary scenarios

with a double period. We ran *vespa* using the TESS light curves detrended with the noise model described in Section 4 and phase-folded using the median values of the posteriors for the period and mid-transit time. The modeled transits of hot Jupiter WASP-132 b were also subtracted from the light curve. We included the maximum possible secondary depth of the phase-folded features calculated by DAVE (Section 2) and the SOAR *I*-band contrast curve (Section 5.1.1) as observational constraints when calculating the FPP of the WASP-132 c signal. By default, *vespa* simulates the background starfield within 1 deg^2 of the target, but we dictated that the maximum aperture radius interior to which the signal must be produced be $42''$, which is the radius of two TESS pixels and the maximum size of the aperture that the SPOC pipeline used to extract the light curves.

Using these inputs, we calculated the FPP of the WASP-132 c signal to be 0.00193. The only false-positive scenario with any remaining probability was the case of a blended background eclipsing binary; however, the probability for that scenario was $\ll 0.01$ and is highly disfavored over the planet scenario. Since the overall FPP $\ll 0.01$, this signal can be considered statistically validated by *vespa*.

As an independent check, we ran the WASP-132 c signal through the statistical validation software TRICERATOPS. This software is similar to *vespa* in that it checks the signal against a set of scenarios that could produce transit-like signals. TRICERATOPS was specifically designed for TESS observations and accounts for known nearby stars contained within the light-curve extraction aperture, as well as stars within 2/5 of the target. This tool calculates both the FPP of the signal and the probability that the planet candidate is a false positive originating from a known nearby star, labeled the nearby FPP (NFPP).

Since TRICERATOPS is sensitive to the extraction aperture, we ran it using light curves extracted with two separate apertures for comparison and quality check. The first run used the apertures that the TESS SPOC pipeline used to extract the PDC_SAP light curves, which were 12 and 10 pixels centered on the target position for Sectors 11 and 38, respectively. The second run used custom light curves extracted using reduced apertures that were smaller than those used by the TESS SPOC pipeline, with 4 and 6 pixels centered on the target position for Sectors 11 and 38, respectively.

For each TRICERATOPS run, we input the apertures used to extract the light curves, the *I*-band contrast curve from SOAR, and the median values for period and mid-transit time from the modeling performed in Section 4. The light curves used were phase-folded at these period and mid-transit time values. For each set of apertures, we ran TRICERATOPS 20 times and took the average FPP values. Using the apertures from the TESS SPOC pipeline, we obtained an $\text{FPP} = 0.0126 \pm 0.0003$ for WASP-132 c. Using the reduced apertures, we obtained an $\text{FPP} = 0.0107 \pm 0.0004$. Since the nearby field has been cleared of nearby and background eclipsing binary systems by the LCOGT observations (see Section 5.1.3), SOAR observations (see Section 5.1.1), and TESS SPOC centroid offset tests (which put the signal within $1'' \pm 3''$ of the target), we assume an NFPP value of zero.

According to Giacalone et al. (2021), for a signal to be statistically validated as a planet by TRICERATOPS, it must have $\text{FPP} < 0.015$. Our signal of 1.01 days meets the TRICERATOPS FPP criterion for both sets of extraction

²⁵ <https://exofop.ipac.caltech.edu/tess/target.php?id=127530399>

apertures. For consistency, we also reran *vespa* on the reduced-aperture light curve and obtained an $FPP = 9.02 \times 10^{-5}$, still well below the *vespa* statistical validation threshold. This difference in FPP between *vespa* and TRICERATOPS may stem from the fact that TRICERATOPS uses the actual TESS aperture and background star population, while *vespa* simulated them with a extraction radius and TRILEGAL simulations. Therefore, given the *vespa* validation, sufficiently low TRICERATOPS FPP values, and strong constraints on nearby background stars in the field of view, we consider this signal to be statistically validated as a planet.

Furthermore, neither of these statistical validation packages account for the fact that this signal is a part of a multiplanet system. Lissauer et al. (2012, 2014) demonstrated that false positives are less likely in multiplanet systems and that the FPPs calculated without accounting for this fact should be treated as upper limits. An analysis of TESS multiplanet systems indicates that this “multiplicity boost” may reduce these FPPs by a factor of $\sim 20\times$ (Guerrero et al. 2021), although the scarcity of inner companions to hot Jupiters suggests that the multiplicity boost should be smaller than this factor.

6. Dynamical Stability

To probe the dynamical stability of the system, we simulated the system using REBOUND (Rein & Liu 2012), a flexible N -body integrator written in both Python and C. We ran 30 iterations of the system, each time perturbing the mass, eccentricity, inclination, and periods of each of the planets within their 3σ uncertainties to test the stability at the extremes of the possible parameter space for both planets. Each iteration was integrated for simulation timescales of 100 Myr and a time step of 0.2 day ($\sim 20\%$ of WASP-132 c’s best-fit orbital period) using the MERCURIUS integrator (Rein et al. 2019).

The MERCURIUS integrator is a hybrid integrator that uses the symplectic Wisdom–Holman integrator WHFast when particles are far apart from each other and switches to the higher-order integrator IAS15 during close encounters, which integrates with a smaller, adaptive time step. We specified the minimum time step for the IAS15 integrator as 0.02 day in order to speed up computation time.

We found that the planetary system is stable for all portions of the parameter space simulated on timescales of 100 Myr. None of the simulations exhibited a drastic change in semimajor axis outside of the normal oscillations due to gravitational interactions between the three bodies in the system (the two planets and the host star). Furthermore, no collisions were registered between any of the bodies over the course of the simulations.

We also simulated the system using the 3σ upper limits on mass, eccentricity, and inclination for both of the planets in order to maximize the likelihood of a close encounter. We integrated this system using the MERCURIUS integrator for 1 Myr at a time step of 1.2 hr ($\sim 5\%$ of WASP-132 c’s best-fit orbital period). The positions of both planets at 1000 different evenly spaced time steps can be seen in Figure 6. We found that the system was stable at the extreme end of the parameter space of both planets, as there were no close encounters between the planets and no significant change in the semimajor axis of the two planets over the course of the simulation. This is illustrated by the gap between the innermost positions of

WASP-132 b and outermost positions of WASP-132 c in Figure 6. Given the stability from both simulations with random draws of parameters, as well as the simulation with the planet parameter values most likely to cause a close encounter, the addition of WASP-132 c into the WASP-132 system does not appear to affect the long-term stability of the system.

7. Discussion

The discovery and validation of WASP-132 c places the WASP-132 system among only a handful of systems with nearby companions to a hot Jupiter. Prior to WASP-132, only WASP-47 (Becker et al. 2015), Kepler-730 (Cañas et al. 2019), and TOI-1130 (Huang et al. 2020) were known to harbor a hot Jupiter with nearby companions. Figure 7 illustrates all of the currently known systems containing hot Jupiters with nearby companions. The existence of these four multiplanet systems is still consistent with occurrence rate estimates provided by Huang et al. 2016; Zhu & Dong 2021, and Hord et al. (2021) which calculate $1.1^{+13.3}_{-1.1}\%$, $\sim 2\%$ ($< 9.7\%$, 95% upper limit), and $7.3^{+15.2}_{-7.3}\%$ of hot Jupiters to have nearby companions, respectively.

7.1. Potential Formation Pathways

The existence of nearby companions in four hot Jupiter systems suggests a dynamically cooler formation mechanism than the high-eccentricity migration that is invoked to explain a significant fraction of hot Jupiters. Although TESS appears to be improving our understanding of the architecture of hot Jupiter systems—now with a second hot Jupiter companion discovery presented here—hot Jupiters with companions are still a rarity, comprising only a small percentage of the nearly 500 hot Jupiters currently confirmed. Few hot Jupiter systems have yet been searched for companions to this level of sensitivity, though. This scarcity of hot Jupiters with nearby companions suggests that high-eccentricity formation scenarios may dominate the observed hot Jupiter population. However, there is increasing evidence that there must be a subpopulation of hot Jupiters that do not form via high-eccentricity migration. This is evidenced not only by the existence of hot Jupiters with nearby companions, as presented here, but also statistical simulations and analytical calculations show that high-eccentricity migration alone cannot reproduce the observed hot Jupiter population and require a mechanism such as disk migration (Dawson et al. 2014; Anderson et al. 2016; Muñoz et al. 2016). Although disk migration could explain this handful of unique systems, it is also possible that a super-Earth could have managed to exceed the threshold mass for runaway gas accretion, forming the hot Jupiter and leaving intact any planets orbiting the interior (Lee et al. 2014; Batygin et al. 2016; Huang et al. 2020).

The subpopulation of hot Jupiters with companions that apparently did not undergo high-eccentricity migration may have more in common with warm Jupiters (10 days $< P < 100$ days) than their fellow hot Jupiters in terms of formation. In contrast to hot Jupiters, $\sim 50\%$ of warm Jupiters have nearby companion planets (Huang et al. 2016). Hot Jupiters with companions form a seemingly continuous period distribution with their warm Jupiter counterparts (Huang et al. 2020) and may represent the tail end of a wider population spanning across the physically unmotivated 10 day dividing line.

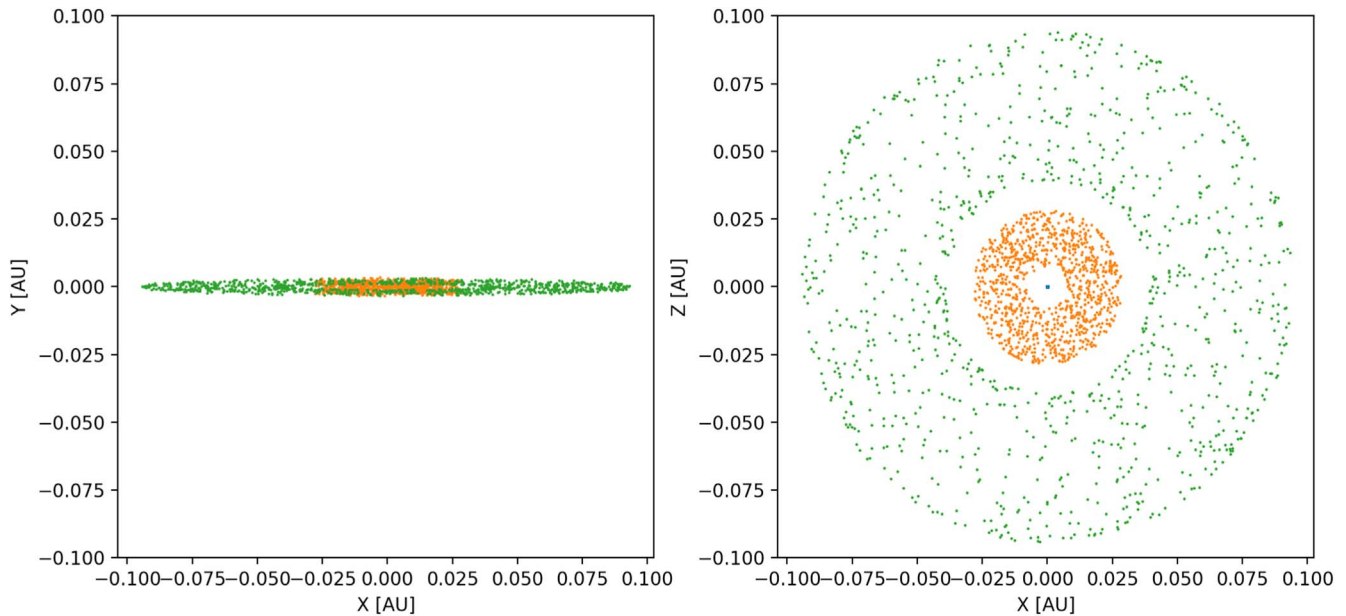


Figure 6. Position of WASP-132 b and c at 1000 evenly spaced points in time during the 1 Myr simulation with mass, eccentricity, and inclination initial values set to the 3σ upper limits for both planets. WASP-132 b is denoted by the outer green points, and WASP-132 c is denoted by the inner orange points. Left: side-on view of the system as it would be seen from Earth. Right: top-down view to illustrate the positions of both planets as they orbit over the course of 1 Myr. Note the gap between the maximum distance of WASP-132 c and the minimum distance of WASP-132 b from the host star.

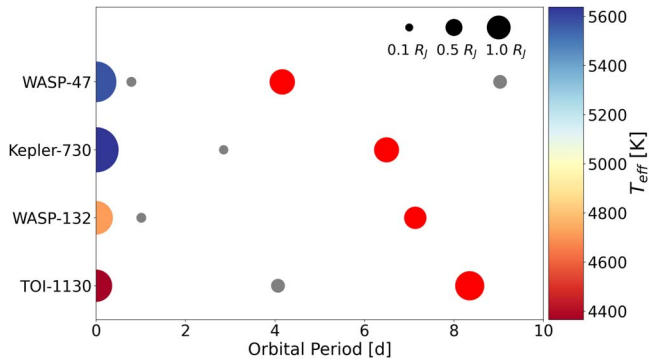


Figure 7. Schematic depiction of the four known systems with a hot Jupiter and at least one nearby companion planet (WASP-47, Kepler-730, TOI-1130, and WASP-132). The orbital periods of the hot Jupiters increase from top to bottom. The sizes of the circles for the planets are to scale with one another but not with the distance from the host star and the host star radius. Likewise, the circles for the host stars are to scale with one another but not with the planets or orbital distance. Hot Jupiters are denoted by red circles, companion planets are denoted by gray circles, and stellar hosts are colored based on their surface temperature.

Taking, for instance, a definition of hot Jupiter based on equilibrium temperature, where $T_{\text{eq}} > 1000$ K defines a hot Jupiter (e.g., Miller & Fortney 2011; Thorngren & Fortney 2018), leaves only WASP-47 b and Kepler-730 b classified as hot Jupiters with T_{eq} of 1259 and 1219 K, respectively, with TOI-1130 b and WASP-132 b classified in a slightly lower “warm” range with T_{eq} of 637 and 763 K, respectively. This definition of hot Jupiters based on equilibrium temperature is equally arbitrary, however, as it still fails to provide a clear distinction between hot Jupiter subpopulations that formed via different formation mechanisms. Systems from a potential “warm Jupiter tail,” such as those discussed here, would inadvertently be included in this definition of hot Jupiters.

7.2. Investigating System Architectures

Comparing these unique systems to the overall exoplanet population (see Figure 8), it becomes apparent that three of the hot Jupiters with nearby companions have orbital periods that are longer than the typical hot Jupiter. The hot Jupiters with companions reside in a more sparsely populated region of period–radius space farther from their host stars than most hot Jupiters. While this is notable, the sample of known hot Jupiters with nearby companions is currently too small to determine if there is a correlation between the presence of a companion and the hot Jupiter orbital or physical properties (or host star type). Furthermore, the cluster of hot Jupiters around an orbital period of 2–3 days is dominated by transit detections, whereas hot Jupiters are quite common on 4–5 day orbits when considering only radial velocity discoveries. Further analysis is required to quantify the extent to which the hot Jupiters with close companions are outliers in the period–radius space.

What we know today is that the known hot Jupiter nearby companions predominantly orbit interior to the hot Jupiter, so the hot Jupiter must orbit at a certain distance from the host star so that there is enough room in the system for a stable orbit of a smaller planet interior to the hot Jupiter. There is the notable exception of the WASP-47 system, which also has one exterior companion. Whether additional exterior transiting companions to hot Jupiters exist remains to be seen, especially given the fact that all of the currently known close companions have been discovered via transits, which are biased toward planets on shorter orbital periods. With the probability of transit dropping with increasing orbital period, the discovery of additional exterior transiting companions is more challenging. Constraints have been placed on the existence of nearby nontransiting planets through the investigation of TTVs using Kepler data, with only WASP-148 c being found (Steffen et al. 2012; Hébrard et al. 2020), supporting the idea that exterior companions are indeed perhaps intrinsically rarer than interior companions. Analysis of comprehensive transit timing searches

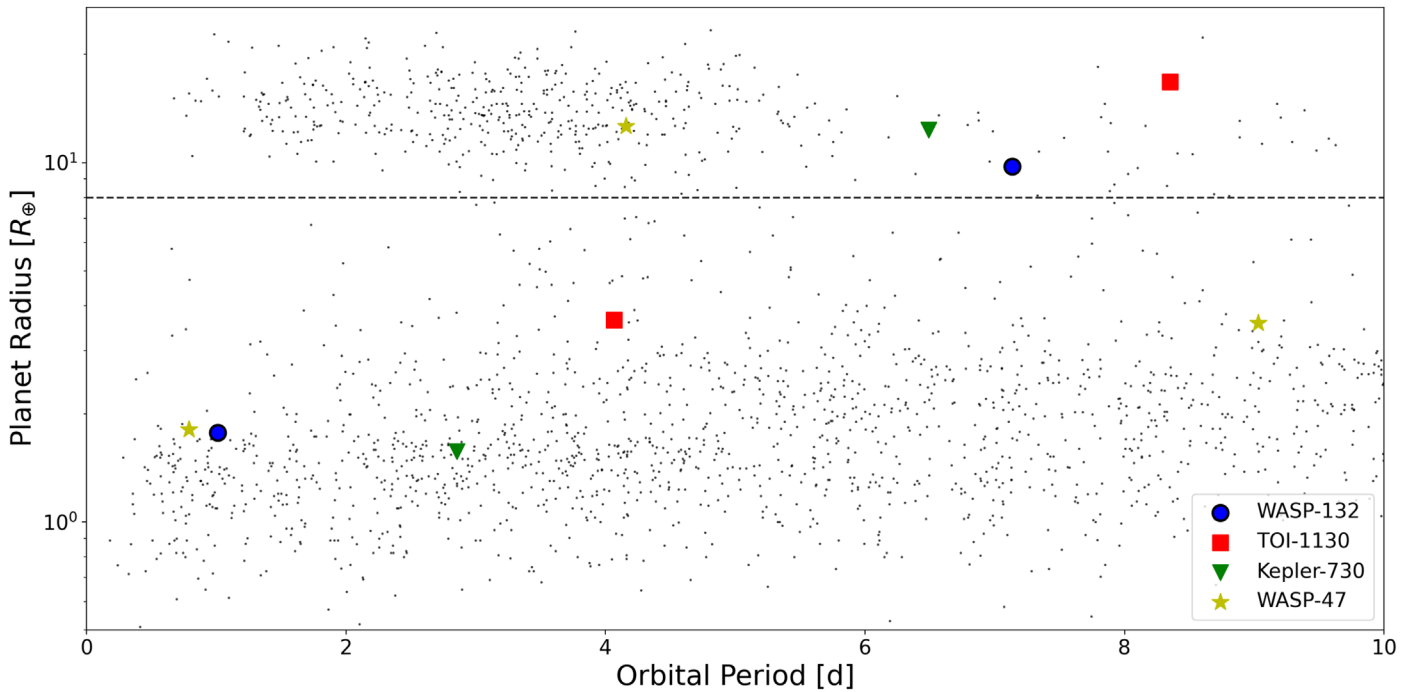


Figure 8. Period and radius of all planets in the four hot Jupiter systems with known companion planets (WASP-47, Kepler-730, TOI-1130, and WASP-132) overlaid on the periods and radii of all planets contained in the NASA Exoplanet Archive. The larger, colored markers represent planets in one of these systems, with similar markers corresponding to planets in the same system. The markers for WASP-132 b and c are outlined in black. A dashed horizontal line has been included at $8 R_{\oplus}$ to denote the division between hot Jupiters and smaller planets.

using TESS data (such as that of Ivshina & Winn 2022) could provide updated constraints, however.

Simulations performed by Ogihara et al. (2013, 2014) have provided a possible explanation for the dearth of external companions. They show that the existence of super-Earths exterior to a hot Jupiter would drive the hot Jupiter into the host star. Therefore, any hot Jupiters with external planets would have been driven into the host star prior to their discovery, thus leading to the “crowding-out of giants by dwarfs,” as Ogihara et al. (2013) referred to it.

In each of the previously known hot Jupiter systems with nearby companions, none of the planets are in orbital resonance with each other. The case is the same for WASP-132. A small fraction of Kepler multiplanet systems are in resonances (Lissauer et al. 2011), whereas wide-orbiting giant planets frequently are (Winn & Fabrycky 2015). Expanding the sample of hot Jupiters with nearby companions would allow for the comparison of the period ratio distribution of hot Jupiters with nearby companions to other known exoplanet populations. Similar distributions of period ratios would be expected from populations of systems that were assembled in a similar manner, and comparing the period ratio distribution of hot Jupiters with companions and the occurrence of resonances to a population such as super-Earth systems could elucidate possible common formation mechanisms.

7.3. Prospects for Follow Up

These hot Jupiters with companions provide a unique opportunity to test if spin-orbit misalignment is a consequence of high-eccentricity migration, as theorized. Based on the derived parameters of the host star and WASP-132 c, we estimate that the semiamplitude of the Rossiter–McLaughlin effect for WASP-132 c is $\sim 0.5 \text{ m s}^{-1}$ (assuming a $v \sin i \sim 0.9$

km s^{-1} , as reported by Hellier et al. 2017). The estimated semiamplitude of the hot Jupiter WASP-132 b is much larger at $\sim 17 \text{ m s}^{-1}$. Although the prospect of measuring the Rossiter–McLaughlin effect for WASP-132 c is quite low, that of WASP-132 b can easily be detected with current radial velocity precision and may inform our understanding of the orbital alignment with the host star’s rotation. The WASP-132 system is otherwise amenable to additional follow-up observations, as it is relatively bright at near-infrared wavelengths ($K_s = 9.674$).

Further radial velocity monitoring and a measured mass are necessary to confirm the planetary nature of this planet. Given that the expected semiamplitude of WASP-132 c is between 3 and 6 m s^{-1} , an instrument more sensitive than CORALIE, such as HARPS or PFS, would be ideal to follow up on WASP-132 c to obtain a mass measurement and further characterize the system. Both of these instruments have 1 m s^{-1} sensitivity or better, making a detection of WASP-132 c with either instrument possible.

8. Summary

In this paper, we present the discovery and validation of a companion planet orbiting interior to the hot Jupiter WASP-132 b. Our investigation and results are summarized as follows.

1. An ~ 1.01 day periodic signal with an FAP $\ll 1\%$ was detected in the TESS photometric data for WASP-132 (TOI-822) with both the SPOC pipeline and the TLS search algorithm. Neither the TESS SPOC pipeline nor the vetting software DAVE found any immediate false-positive indicators.
2. We refined the system parameters, obtaining a host star of $R_* = 0.753^{+0.028}_{-0.026} R_{\odot}$ and $M_* = 0.782 \pm 0.034 M_{\odot}$ and planets with periods and radii of 7.13 days and

- 10.05 ± 0.28 R_{\oplus} for WASP-132 b and 1.01 days and 1.85 ± 0.10 R_{\oplus} for WASP-132 c.
- An analysis of archival CORALIE radial velocity measurements did not yield a significant detection at the 1.01 day period, with a 3σ upper limit of 37.35 M_{\oplus} on the mass of WASP-132 c.
 - Using LCOGT ground-based follow-up photometry, we ruled out NEB signals as the potential source of the TESS detection in stars out to 50'' from WASP-132 c and likely ruled out potential NEB signals in stars out to 2'.5.
 - WASP-132 c is statistically validated as a planet with FPPs of 9.02×10^{-5} and 0.0107 using *vespa* and TRICERATOPS, respectively (see Section 5.2 for further discussion).
 - The system is dynamically stable on timescales of 100 Myr for planetary and orbital parameters within 3σ of the best-fit values.
 - WASP-132 is the second system discovered by TESS (and one of only four systems in total) to contain a hot Jupiter with a nearby companion planet, suggesting that a mechanism other than high-eccentricity migration may play a significant role in the formation of hot Jupiters.

The discovery of WASP-132 c demonstrates the ability of TESS to not only find new planets but also enhance our knowledge of those already known. As TESS continues its almost-all-sky survey, it will surely reveal additional systems similar to WASP-132 that will improve our understanding of the evolution of hot Jupiter systems. With an ever-expanding census of hot Jupiters with nearby companion planets, it may even be possible to identify subpopulations of these hot, giant planets. It is imperative to continue the search for this type of system architecture, as a larger data set will allow us to solidify our understanding of how these rare systems form.

We thank J. Rowe and T. Barclay for the valuable suggestions for this study.

This paper includes data collected by the TESS mission, which are publicly available from the Mikulski Archive for Space Telescopes (MAST) and produced by the Science Processing Operations Center (SPOC) at NASA Ames Research Center. This research effort made use of systematic error-corrected (PDC-SAP) photometry. Funding for the TESS mission is provided by NASA's Science Mission directorate.

Resources supporting this work were provided by the NASA High-End Computing (HEC) Program through the NASA Advanced Supercomputing (NAS) Division at Ames Research Center for the production of the SPOC data products.

This research has made use of the Exoplanet Followup Observation Program website, which is operated by the California Institute of Technology, under contract with the National Aeronautics and Space Administration under the Exoplanet Exploration Program.

This work has made use of data from the European Space Agency (ESA) mission Gaia (<https://www.cosmos.esa.int/gaia>), processed by the Gaia Data Processing and Analysis Consortium (DPAC; <https://www.cosmos.esa.int/web/gaia/dpac/consortium>). Funding for the DPAC has been provided by national institutions, in particular the institutions participating in the Gaia Multilateral Agreement.

This publication makes use of the Data & Analysis Center for Exoplanets (DACE), which is a facility based at the University of Geneva (CH) dedicated to extrasolar planet data

visualization, exchange, and analysis. DACE is a platform of the Swiss National Centre of Competence in Research (NCCR) PlanetS, federating the Swiss expertise in exoplanet research. The DACE platform is available at <https://dace.unige.ch>.

Simulations in this paper made use of the REBOUND *N*-body code (Rein & Liu 2012). The simulations were integrated using the hybrid symplectic MERCURIUS integrator (Rein et al. 2019).

This work makes use of observations from the LCOGT network. Part of the LCOGT telescope time was granted by NOIRLab through the Mid-Scale Innovations Program (MSIP). MSIP is funded by NSF.

B.J.H. acknowledges support from the Future Investigators in NASA Earth and Space Science and Technology (FINESST) program grant 80NSSC20K1551 and support by NASA under award No. 80GSFC21M0002. T.A.B. and M.L.S. acknowledge support from an appointment to the NASA Postdoctoral Program at the NASA Goddard Space Flight Center, administered by the Universities Space Research Association and Oak Ridge Associated Universities under contract with NASA.

Facilities: CORALIE, Gaia, LCOGT, SOAR, TESS.

Software: AstroImageJ (Collins et al. 2017), astropy (Robitaille et al. 2013; Price-Whelan et al. 2018), celerite (Foreman-Mackey et al. 2017; Foreman-Mackey 2018), DACE, DAVE (Kostov et al. 2019b), exoplanet (Foreman-Mackey et al. 2019), Forecaster (Chen & Kipping 2016), Jupyter (Kluyver et al. 2016), Lightkurve (Lightkurve Collaboration et al. 2018), matplotlib (Hunter 2007), NumPy (Van Der Walt et al. 2011), Pandas (McKinney 2010), PyMC3 (Salvatier et al. 2016), SciPy (Oliphant 2007), STARRY (Luger et al. 2018; Agol et al. 2019), TAPIR (Jensen 2013), Theano (Theano Development Team 2016), TRICERATOPS (Giacalone & Dressing 2020; Giacalone et al. 2021), REBOUND (Rein & Liu 2012), *vespa* (Morton 2012, 2015).

ORCID iDs

Benjamin J. Hord  <https://orcid.org/0000-0001-5084-4269>
 Nicole D. Colón  <https://orcid.org/0000-0001-8020-7121>
 Travis A. Berger  <https://orcid.org/0000-0002-2580-3614>
 Veselin Kostov  <https://orcid.org/0000-0001-9786-1031>
 Michele L. Silverstein  <https://orcid.org/0000-0003-2565-7909>
 Keivan G. Stassun  <https://orcid.org/0000-0002-3481-9052>
 Jack J. Lissauer  <https://orcid.org/0000-0001-6513-1659>
 Karen A. Collins  <https://orcid.org/0000-0001-6588-9574>
 Richard P. Schwarz  <https://orcid.org/0000-0001-8227-1020>
 Ramotholo Sefako  <https://orcid.org/0000-0003-3904-6754>
 Carl Ziegler  <https://orcid.org/0000-0002-0619-7639>
 César Briceño  <https://orcid.org/0000-0001-7124-4094>
 Nicholas Law  <https://orcid.org/0000-0001-9380-6457>
 Andrew W. Mann  <https://orcid.org/0000-0000-3654-1602>
 George R. Ricker  <https://orcid.org/0000-0003-2058-6662>
 David W. Latham  <https://orcid.org/0000-0001-9911-7388>
 S. Seager  <https://orcid.org/0000-0002-6892-6948>
 Joshua N. Winn  <https://orcid.org/0000-0002-4265-047X>
 Jon M. Jenkins  <https://orcid.org/0000-0002-4715-9460>
 Luke G. Bouma  <https://orcid.org/0000-0002-0514-5538>
 Guillermo Torres  <https://orcid.org/0000-0002-5286-0251>
 Joseph D. Twicken  <https://orcid.org/0000-0002-6778-7552>
 Andrew Vanderburg  <https://orcid.org/0000-0001-7246-5438>

References

- Agol, E., Luger, R., & Foreman-Mackey, D. 2019, *AJ*, 159, 123
- Allard, F., Homeier, D., & Freytag, B. 2012, *RSPTA*, 370, 2765
- Anderson, K. R., Storch, N. I., & Lai, D. 2016, *MNRAS*, 456, 3671
- Bailer-Jones, C. A. L., Rybizki, J., Founesneau, M., Mantelet, G., & Andrae, R. 2018, *AJ*, 156, 58
- Barclay, T., Pepper, J., & Quintana, E. V. 2018, *ApJS*, 239, 2
- Batygin, K., Bodenheimer, P. H., & Laughlin, G. P. 2016, *ApJ*, 829, 114
- Becker, J. C., Vanderburg, A., Adams, F. C., Rappaport, S. A., & Schwengel, H. M. 2015, *ApJL*, 812, L18
- Berger, T. A., Huber, D., van Saders, J. L., et al. 2020, *AJ*, 159, 280
- Bovy, J., Rix, H.-W., Green, G. M., Schlafly, E. F., & Finkbeiner, D. P. 2016, *ApJ*, 818, 130
- Brown, A. G., Vallenari, A., Prusti, T., et al. 2021, *A&A*, 649, A1
- Brown, T. M., Baliber, N., Bianco, F. B., et al. 2013, *PASP*, 125, 1031
- Cañas, C. I., Wang, S., Mahadevan, S., et al. 2019, *ApJL*, 870, L17
- Chen, J., & Kipping, D. 2016, *ApJ*, 834, 17
- Collins, K. A., Kielkopf, J. F., Stassun, K. G., & Hessman, F. V. 2017, *AJ*, 153, 77
- Coughlin, J. L., Thompson, S. E., Bryson, S. T., et al. 2014, *AJ*, 147, 119
- Crossfield, I. J. M., Waalkes, W., Newton, E. R., et al. 2019, *ApJL*, 883, L16
- Cutri, R. M., Wright, E. L., Conrow, T., et al. 2013, Explanatory Supplement to the AllWISE Data Release Products (Washington, DC: NASA)
- Dawson, R. I., & Johnson, J. A. 2018, *ARA&A*, 56, 175
- Dawson, R. I., Murray-Clay, R. A., & Johnson, J. A. 2014, *ApJ*, 798, 66
- de Leon, J. P., Livingston, J., Endl, M., et al. 2021, *MNRAS*, 508, 195
- Dieterich, S. B., Henry, T. J., Jao, W.-C., et al. 2014, *AJ*, 147, 94
- Endl, M., Caldwell, D. A., Barclay, T., et al. 2014, *ApJ*, 795, 151
- ExoFOP 2019, AAS Meeting, 233, 140.09
- Foreman-Mackey, D. 2018, *RNAAS*, 2, 31
- Foreman-Mackey, D., Agol, E., Ambikasaran, S., & Angus, R. 2017, *AJ*, 154, 220
- Foreman-Mackey, D., Czekala, I., Luger, R., et al. 2019, *dfm/exoplanet* v0.2.3, Zenodo, doi:10.5281/zenodo.1998447
- Gaia Collaboration, Brown, A. G. A., Vallenari, A., et al. 2018, *A&A*, 616, A1
- Garhart, E., Deming, D., Mandell, A., et al. 2020, *AJ*, 159, 137
- Giacalone, S., & Dressing, C. D. 2020, triceratops: Candidate Exoplanet Rating Tool, Astrophysics Source Code Library, ascl:2002.004
- Giacalone, S., Dressing, C. D., Jensen, E. L. N., et al. 2021, *AJ*, 161, 24
- Gilbert, E. A., Barclay, T., Schlieder, J. E., et al. 2020, *AJ*, 160, 116
- Guerrero, N. M., Seager, S., Huang, C. X., et al. 2021, *ApJS*, 254, 39
- Hébrard, G., Díaz, R., Correia, A., et al. 2020, *A&A*, 640, A32
- Hedges, C., Saunders, N., Barentsen, G., et al. 2019, *ApJL*, 880, L5
- Heller, C., Anderson, D. R., Collier Cameron, A., et al. 2017, *MNRAS*, 465, 3693
- Henden, A. A., Templeton, M., Terrell, D., et al. 2016, *yCat*, II/336
- Hipke, M., & Heller, R. 2019, *A&A*, 623, A39
- Hoffman, M. D., Gelman, A., et al. 2014, *J. Mach. Learn. Res.*, 15, 1593, <http://jmlr.org/papers/v15/hoffman14a.html>
- Hord, B. J., Colón, K. D., Kostov, V., et al. 2021, *AJ*, 162, 263
- Huang, C., Wu, Y., & Triaid, A. H. 2016, *ApJ*, 825, 98
- Huang, C. X., Quinn, S. N., Vanderburg, A., et al. 2020, *ApJL*, 892, L7
- Huber, D., Zinn, J., Bojsen-Hansen, M., et al. 2017, *ApJ*, 844, 102
- Hunter, J. D. 2007, *CSE*, 9, 90
- Ivshina, E. S., & Winn, J. N. 2022, *ApJS*, 259, 62
- Jenkins, J. M. 2002, *ApJ*, 575, 493
- Jenkins, J. M., Tenenbaum, P., Seader, S., et al. 2020, Kepler Science Document KSCI-19081-003, 9
- Jenkins, J. M., Chandrasekaran, H., McCauliff, S. D., et al. 2010, *Proc. SPIE*, 7740, 77400D
- Jenkins, J. M., Twicken, J. D., McCauliff, S., et al. 2016, *Proc. SPIE*, 9913, 99133E
- Jensen, E. 2013, Tapir: A web interface for transit/eclipse observability, Astrophysics Source Code Library, ascl:1306.007
- Kipping, D. M. 2013a, *MNRAS*, 435, 2152
- Kipping, D. M. 2013b, *MNRASL*, 434, L51
- Kluyver, T., Ragan-Kelley, B., Pérez, F., et al. 2016, in Positioning and Power in Academic Publishing: Players, Agents and Agendas, ed. F. Loizides & B. Schmidt (Amsterdam: IOS Press), 87
- Knutson, H. A., Fulton, B. J., Montet, B. T., et al. 2014, *ApJ*, 785, 126
- Kostov, V. B., Mullally, S. E., Quintana, E. V., et al. 2019a, *AJ*, 157, 124
- Kostov, V. B., Schlieder, J. E., Barclay, T., et al. 2019b, *AJ*, 158, 32
- Kovács, G., Zucker, S., & Mazeh, T. 2002, *A&A*, 391, 369
- Lee, E. J., Chiang, E., & Ormel, C. W. 2014, *ApJ*, 797, 95
- Lee, M. H., & Peale, S. J. 2002, *ApJ*, 567, 596
- Li, J., Tenenbaum, P., Twicken, J. D., et al. 2019, *PASP*, 131, 024506
- Lightkurve Collaboration, Cardoso, J. V. d. M., Hedges, C., et al. 2018, Lightkurve: Kepler and TESS time series analysis in Python, Astrophysics Source Code Library, ascl:1812.013
- Lin, D. N., Bodenheimer, P., & Richardson, D. C. 1996, *Natur*, 380, 606
- Lissauer, J. J., Ragozzine, D., Fabrycky, D. C., et al. 2011, *ApJS*, 197, 8
- Lissauer, J. J., Marcy, G. W., Rowe, J. F., et al. 2012, *ApJ*, 750, 112
- Lissauer, J. J., Marcy, G. W., Bryson, S. T., et al. 2014, *ApJ*, 784, 44
- Lovis, C., & Fischer, D. A. 2011, in Exoplanets, ed. S. Seager (Tucson, AZ: Univ. of Arizona Press), 27
- Luger, R., Agol, E., Foreman-Mackey, D., et al. 2018, *AJ*, 157, 64
- Luger, R., Agol, E., Foreman-Mackey, D., et al. 2019, *AJ*, 157, 64
- Mamajek, E. E., & Hillenbrand, L. A. 2008, *ApJ*, 687, 1264
- Mayor, M., & Queloz, D. 1995, *Natur*, 378, 355
- McCully, C., Volgenau, N. H., Harbeck, D.-R., et al. 2018, *Proc. SPIE*, 10707, 107070K
- McKinney, W. 2010, in Proc. of the 9th Python in Science Conf. 51, ed. S. van der Walt & J. Millman
- Miller, N., & Fortney, J. J. 2011, *ApJL*, 736, L29
- Morton, T. D. 2012, *ApJ*, 761, 6
- Morton, T. D. 2015, VESPA: False positive probabilities calculator, Astrophysics Source Code Library, ascl:1503.011
- Muñoz, D. J., Lai, D., & Liu, B. 2016, *MNRAS*, 460, 1086
- Mustill, A. J., Davies, M. B., & Johansen, A. 2015, *ApJ*, 808, 14
- Ogihara, M., Inutsuka, S.-i., & Kobayashi, H. 2013, *ApJL*, 778, L9
- Ogihara, M., Kobayashi, H., & Inutsuka, S. I. 2014, *ApJ*, 787, 172
- Oliphant, T. E. 2007, *CSE*, 9, 10
- Price-Whelan, A. M., Sipőcz, B., Günther, H., et al. 2018, *AJ*, 156, 123
- Prusti, T., De Bruijne, J., Brown, A. G., et al. 2016, *A&A*, 595, A1
- Rasio, F. A., & Ford, E. B. 1996, *Sci*, 274, 954
- Raymond, S. N., Mandell, A. M., & Sigurdsson, S. 2006, *Sci*, 313, 1413
- Rein, H., & Liu, S. F. 2012, *A&A*, 537, A128
- Rein, H., Hernandez, D. M., Tamayo, D., et al. 2019, *MNRAS*, 485, 5490
- Ricker, G. R. 2015, *BAAS*, 47, 6
- Rickman, E., Ségransan, D., Marmier, M., et al. 2019, *A&A*, 625, A71
- Robitaille, T. P., Tollerud, E. J., Greenfield, P., et al. 2013, *A&A*, 558, A33
- Salvatier, J., Wiecki, T. V., & Fonnesbeck, C. 2016, *PeerJ Comp. Sci.*, 2, e55
- Schlaufman, K. C., & Winn, J. N. 2016, *ApJ*, 825, 62
- Silverstein, M. L., Schlieder, J. E., Barclay, T., et al. 2022, *AJ*, 163, 151
- Skrutskie, M. F., Cutri, R. M., Stiening, R., et al. 2006, *AJ*, 131, 1163
- Smith, J. C., Stumpe, M. C., Van Cleve, J. E., et al. 2012, *PASP*, 124, 1000
- Stassun, K. G., Collins, K. A., & Gaudi, B. S. 2017, *AJ*, 153, 136
- Stassun, K. G., Corsaro, E., Pepper, J. A., & Gaudi, B. S. 2018, *AJ*, 155, 22
- Stassun, K. G., & Torres, G. 2016, *AJ*, 152, 180
- Stassun, K. G., & Torres, G. 2021, *ApJL*, 907, L33
- Stassun, K. G., Oelkers, R. J., Pepper, J., et al. 2018, *AJ*, 156, 102
- Stassun, K. G., Oelkers, R. J., Paegert, M., et al. 2019, *AJ*, 158, 138
- Steffen, J. H., Ragozzine, D., Fabrycky, D. C., et al. 2012, *PNAS*, 109, 7982
- Stumpe, M. C., Smith, J. C., Catanzarite, J. H., et al. 2014, *PASP*, 126, 100
- Stumpe, M. C., Smith, J. C., Van Cleve, J. E., et al. 2012, *PASP*, 124, 985
- Sullivan, P. W., Winn, J. N., Berta-Thompson, Z. K., et al. 2015, *ApJ*, 809, 77
- Theano Development Team 2016, arXiv:1605.02688
- Thorngren, D. P., & Fortney, J. J. 2018, *AJ*, 155, 214
- Tokovinin, A. 2018, *PASP*, 130, 035002
- Torres, G., Andersen, J., & Giménez, A. 2010, *A&ARv*, 18, 67
- Twicken, J. D., Catanzarite, J. H., Clarke, B. D., et al. 2018, *PASP*, 130, 064502
- Van Der Walt, S., Colbert, S. C., & Varoquaux, G. 2011, *CSE*, 13, 22
- Wang, J., Fischer, D. A., Horch, E. P., & Huang, X. 2015, *ApJ*, 799, 229
- Winn, J. N., Fabrycky, D., Albrecht, S., & Johnson, J. A. 2010, *ApJL*, 718, L145
- Winn, J. N., & Fabrycky, D. C. 2015, *ARA&A*, 53, 409
- Wright, E. L., Eisenhardt, P. R., Mainzer, A. K., et al. 2010, *AJ*, 140, 1868
- Yee, S. W., Winn, J. N., & Hartman, J. D. 2021, *AJ*, 162, 240
- Zhu, W., & Dong, S. 2021, *ARA&A*, 59, 291
- Ziegler, C., Tokovinin, A., Briceño, C., et al. 2020, *AJ*, 159, 19